# Inelastic rotations and plastic turbulence

R. Baggio, O U Salman, L. Truskinovsky

# Inelastic rotations and plastic turbulence

R. Baggio,[1, 2, 3] O. U. Salman,[1] and L. Truskinovsky[2]

[1]*LSPM,CNRS UPR3407, Paris Nord Sorbonne Université, 93400, Villateneuse, France*
[2]*PMMH,CNRS UMR 7636 ESPCI ParisTech, 10 Rue Vauquelin,75005, Paris, France*
[3]*UMR SPE 6134, Université de Corse, CNRS, Campus Grimaldi, 20250, Corte, France*

Plastic deformations in crystals often produce textures in the form of randomly oriented patches of the unstressed lattice. We use a novel mesoscopic Landau model of crystal plasticity to show that in such textures particularly large crystallographic lattice rotations originate from inelastic slip at the microscale. Our numerical experiments suggest that the process of the formation of plastic textures is inherently unstable and involves quasi-turbulent motions with power-law distributed spatial correlations.

The emerging experimental evidence of intermittent avalanches and scale-free dislocation patterns triggered a shift from macro- to micro-scale modeling efforts in crystal plasticity [1–3]. The recorded temporal and spatial correlations were interpreted as evidence of cooperative dynamics at sub-continuum scales [4–6], and the observed hierarchically organized deformation fields were likened to scale-free turbulent flows [7–12]. Since fluid turbulence largely relies on vortices, the question arises whether large rotations play similarly crucial role in crystal plasticity [13–17].

When crystalline specimens are deformed plastically, small elastic rotations are known to be necessary to ensure lattice compatibility [18, 19]. The energetically neutrality rigid rotations are also used to explain the localization of dislocations in wall structures [20–25]. Yet, the actual microscopic mechanism of large rotations involved in some of the ensuing textures remains obscure.

New insights emerged from recent molecular dynamic simulations of single-crystal plasticity suggesting that the patchy local reorientation of the crystal lattice may be due to deformation induced micro- or nano-twinning [26–30]. In physical experiments similar effects were found, for instance, in [31, 32]. In this Letter, we corroborate the idea of inelastic rotations theoretically and show explicitly how some crystallographically specific collective micro-deformations of twinning type can disguise themselves as large crystal rotations.

Our main tool is the novel mesoscopic tensorial model of crystal plasticity [33, 34]. It represents a crystal as a collection of finite elements whose deformation is governed by periodic potentials. The latter are designed to respect the geometrically nonlinear kinematics of the lattice, as originally envisioned in [35–41]. From the perspective of the resulting Landau theory with an infinite number of energy wells, plastically deformed crystals represent coherent mixtures of equivalent 'phases' [34, 42]. The corresponding computational approach to crystal plasticity bears some resemblance to the local version of the quasi-continuum model [43–45] and also has features in common with tensorial generalizations of the phase-field approach to dislocational plasticity [46–50].

As a proof of principle, in this Letter, we studied in detail a single plastic avalanche resulting from a brittle-like yield of a homogeneously deformed pristine crystal [42]. During such an event, multiple dislocations nucleate collectively, and the lattice rearranges itself into patches of the original lattice with different orientations. Our numerical experiments provided a compelling evidence that in most of such patches, the apparent rigid rotations are achieved through distributed lattice invariant shears resulting in the formation of micro-twinned laminates. The idea of energy minimizing *macro*-scale laminates in crystal plasticity has been already explored in [51, 52], and here we show that such laminates can already form at the *micro*-scale. Moreover, by tracking the deformation history of individual elements, we were able to show that the underlying micro-twins self-organize to appear as macro-rotations. Therefore, the resulting macroscale textures are fundamentally inelastic as they ultimately emerge from the collective motion of dislocations at the microscale.

Furthermore, our numerical experiments suggest that the formation of disoriented patches of the unstressed lattice during discontinuous avalanches is inherently unstable even though the sizes and the misorientations of the individual patches remain correlated. These observations are reminiscent of fluid turbulence and point towards the necessity of probabilistic description of crystal plasticity.

To emphasize ideas, we limit our analysis to the simplest nontrivial 2D problem. We represent the crystal as a collection of $N^2$ discrete elements organized in a square lattice. The internal scale of order $N^{-1}$ is viewed as a physical parameter defining the (Kolmogorov-type) cut-off beyond which the deformation is considered homogeneous. To describe continuum deformation of such lattice we introduce the piecewise smooth mapping $\mathbf{y} = \mathbf{y}(\mathbf{x})$, where $\mathbf{y}$ are actual and $\mathbf{x}$ are reference coordinates. We then associate with each element an elastic energy density $\phi$ which depends on the metric tensor $\mathbf{C} = \mathbf{F}^T\mathbf{F}$, where $\mathbf{F} = \boldsymbol{\nabla}\mathbf{y}$ is the deformation gradient.

In view of the presence of lattice invariant shears, the function $\phi(\mathbf{C})$ takes the form of a multi-well (periodic) Landau potential. It can be computed from a microscale theory using the Cauchy-Born local homogeneity hypothesis [53]. For instance, if $V$ is a pairwise potential, we can write $\phi(\mathbf{C}) = \Omega_0^{-1}\sum_r V(r\,(\mathbf{C}))$, where $r$ is the distance between the sites of the deformed lattice and

$\Omega_0$ is a representative volume, see [54] for details. As the representative volume increases, the function $\phi(\mathbf{C})$ develops a periodic structure with minima associated with lattice invariant shears [55, 56]. In view of the emerging symmetry, $\phi(\mathbf{C}) = \phi(\mathbf{m}^\mathbf{T}\mathbf{C}\mathbf{m})$ where $\mathbf{m}$ is a matrix with integral entries and determinant $\pm 1$, the space of metric tensors $\mathbf{C}$ describing area preserving deformations ($\det \mathbf{C} = 1$) partitions into equivalent domains. Therefore, after the function $\phi(\mathbf{C})$ is known in one of such domains, say $D = \{0 < C_{11} \leq C_{22}, \quad 0 \leq C_{12} \leq C_{11}/2\}$, it can be extended by symmetry [34].

To visualize the implied tensorial periodicity of the function $\phi(\mathbf{C})$, it is convenient to stereo-graphically project the hyperbolic surface $\det \mathbf{C} = 1$ on a 2D disk of unit radius (Poincaré disk), see [54] for details. The resulting tessellation of the configuration space is illustrated in Fig. 1(a); for the graph theory and the crystallographic aspects of the underlying energy wells structure, see [49, 57]. The particular periodic energy landscape used in subsequent numerical experiments, is illustrated in Fig. 1(b); it is based on an interatomic potential from the literature constructed to ensure that the ground state is a square lattice [58].

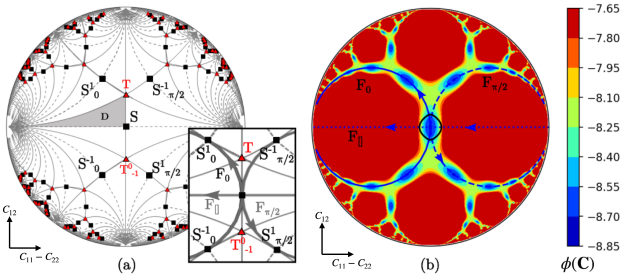


FIG. 1: (a) The configurational space of metric tensors with $\det \mathbf{C} = 1$ (Poincaré disc). Infinite families of equivalent square and triangular lattices are shown by squares $\mathbf{S}$ and triangles $\mathbf{T}$, respectively; $\mathbf{D}$ is the minimal periodicity domain; (b) The energy landscape obtained using an interatomic potential from [58]; a cutoff was applied to improve the visibility of the low-energy valleys. Blue circles: simple shears paths $\mathbf{F}(\alpha, 0)$ (continuous) and $\mathbf{F}(\alpha, \pi/2)$ (dashed). Dotted straight line: pure shear path $\mathbf{F}_{[]}(\alpha)$. The dark oval in (b) represents the effective yield surface.

The low energy valleys in the ensuing (constitutive) landscape correspond to simple shears $\mathbf{F}(\alpha, \theta) = \mathbf{I} + \alpha \mathbf{R}(\theta)\mathbf{e}_1 \otimes \mathbf{e}_2$, where $\mathbf{e}_i$ is the orthonormal basis of the reference lattice, $\mathbf{R}(\theta)$ is a counter-clockwise rotation by the angle $\theta$, and $\alpha$ is the magnitude of the shear. Conventional plastic 'mechanisms' for a square lattice correspond to $\theta = 0, \pi/2$ and the associated simple shears are aligned along the two close packed crystallographic (slip) planes; as $\alpha$ varies, the corresponding metric tensors $\mathbf{C}$ trace circular trajectories, see Fig. 1(b). The matrices $\mathbf{F}(\alpha, 0)$ and $\mathbf{F}(\alpha, \pi/2)$ with *integer* entries correspond to lattice invariant shears and mark the bottoms of the equivalent energy wells.

A pristine crystal, represented by a homogeneous square domain made by NxN elements aligned with coordinate axes, was loaded quasi-statically in a hard device by applying on the boundary incremental affine deformation while performing incremental energy minimization, see [42] for the details on the numerical implementation. We used the 'hard' loading path corresponding to pure shear

$$\mathbf{F}_{[]}(\alpha) = \begin{bmatrix} \cosh(\frac{\alpha}{2}) - \sinh(\frac{\alpha}{2}) & 0 \\ 0 & \cosh(\frac{\alpha}{2}) + \sinh(\frac{\alpha}{2}) \end{bmatrix} \quad (1)$$

This mapping transforms squares into rectangles and we rely here on its natural parametrization $\alpha = 2\log(\lambda)$, where $(\lambda, \lambda^{-1})$ are the two principal stretches [59]; the corresponding path in the configurational space is shown by the dashed line in Fig. 1(b).

A dislocation free crystal, loaded along (1), follows the elastic branch of equilibrium as long as the latter remains stable. The branch switching event (dislocation avalanche) takes place at a critical value of the loading parameter $\alpha$ which can be approximated using the macroscopic Legendre-Hadamard criterion $\det \mathbf{A} = \mathbf{0}$, where $A_{ik} = \mathsf{a}_{ijkl} n_j n_k$ is the acoustic tensor and $\mathsf{a}_{ijkl} = F_{jR}F_{lS}\partial^2\varphi/\partial F_{iR}\partial F_{kS}$ is the Eulerian tensor of elastic moduli [60, 61]. A union of such (spinodal) thresholds for a family of loading paths can be viewed as representing an effective "yield surface", see the black oval around the reference state in Fig. 1(b).

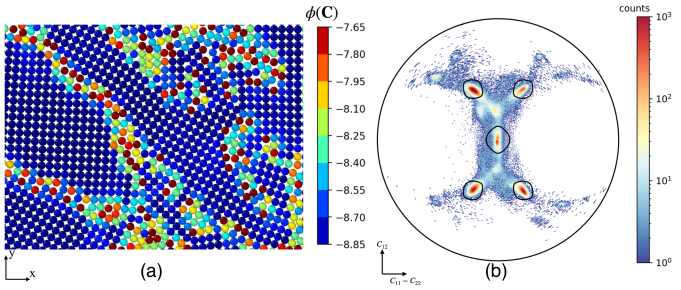


FIG. 2: (a) A fragment of the post-avalanche pattern in real space; colors indicate the level of energy. (b) The distribution of elements in the configurational space for the whole post-avalanche pattern obtained by counting the number of elements inside individual configurational bins. The dark ovals in (b) show the effective yield surfaces around the equivalent energy wells (pristine crystal and its four copies obtained by the smallest lattice invariant shears).

The empirically obtained instability threshold along the loading path $\mathbf{F}_{[]}(\alpha)$ is $\alpha_c \approx 0.176$ which is in excellent agreement with the theoretical prediction; the critical orientation of the unstable mode $\mathbf{n}$ practically coincides with predicted value $\mathbf{e}_1^0$ and the direction of shear (polarization vector) is almost parallel to the theoretically predicted direction $\mathbf{e}_2^0$.

The breakdown of the affine state takes the form of an abrupt drop of both stress and energy as the homogeneously deformed lattice is replaced by a complex texture of disoriented patches of the unstressed lattice, see the fragment in Fig. 2 (a). Our Fig. 2 (b) shows the post-avalanche distribution of the deformed elements in

the configurational space (Poincaré disk). During the avalanche, some of the rectangular (stretched) elements snap back to the reference well $\mathbf{S}$, however, the majority of the elements redistribute among the four neighboring wells; $\mathbf{S}^0_1 = \mathbf{F}(1,0)$, $\mathbf{S}^0_{-1} = \mathbf{F}(-1,0)$, $\mathbf{S}^{\pi/2}_1 = \mathbf{F}(1,\pi/2)$ and $\mathbf{S}^{\pi/2}_{-1} = \mathbf{F}(-1,\pi/2)$. While the first two of these wells correspond to the same slip system, the presence of the other two indicates the parallel activation of the complimentary slip system. Some elements appear to be locked in the shallow local minima $\mathbf{T}$ and $\mathbf{T^0_{-1}}$ describing the triangular lattice with hexagonal symmetry; such elements appear mostly as the components of Shockley-type partials [62]. The limited overall spreading of the elements beyond the low energy valleys reflects the presence of dislocation cores and other highly inhomogeneous defect structures.

The ensuing large scale post-avalanche pattern in the *physical* space is illustrated in Fig. 3(a); for the transients, see Movies S1 and S2 in [54]. Upon magnification we see a complex arrangement of apparently randomly rotated unstressed square lattice patches circumscribed by dislocated boundaries, see Fig. 3(b-d); the fragments of triangular lattice serve as elements of the stacking fault-type interfaces. As we show in [54], the emerging patterns at small scales are qualitatively similar to the ones obtained in molecular statics simulations employing the same interatomic potential.

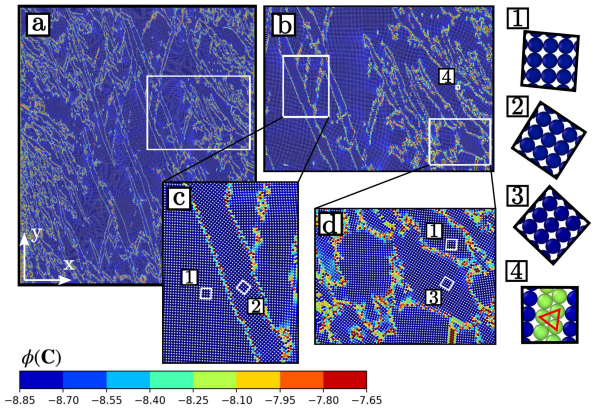


FIG. 3: Post-avalanche pattern shown at different scales. Colors indicate the level of energy. Insets (1-3): relative rotation of unstressed square patches. Inset (4): a fragment of a metastable triangular lattice. Here N=600.

The microscopic nature of large rotations in Fig. 3 can be understood if we follow the deformation of the individual elements. In Fig. 4 we show two representative fragments of the distorted network of such elements illustrating different types of interfaces between misaligned patches of the original lattice.

The elemental triangulation in Fig. 4(a), showing coexisting patches of the type 1-3, reveals that an apparent rigid rotation at the macroscale is, in fact, a disguised micro-twin mixture of the elements of the types

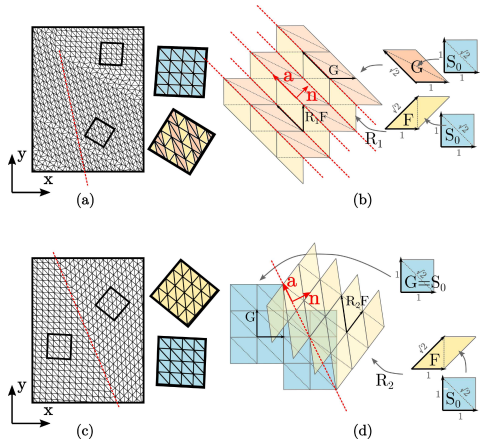


FIG. 4: Magnified fragments of the post-avalanche pattern from Fig. 3 showing the actual affine distortions of individual elements; (a) patches of the type 1-3, (c) patches of the type 1-2; (b,d) illustration of the corresponding solutions of the compatibility equation, see [54] for more details.

$\mathbf{R}(\pi/2)\mathbf{S}^0_1$ and $\mathbf{S}^0_{-1}$. To build such a laminate involving symmetry related deformation gradients $\mathbf{F}$ and $\mathbf{G}$, the latter must satisfy the compatibility condition $\mathbf{RF} = (\mathbf{I} + \mathbf{a} \otimes \mathbf{n})\,\mathbf{G}$, where $\mathbf{R}$ is a rotation and $\mathbf{a} \cdot \mathbf{n} = 0$ [63]. The necessary condition for the existence of such $\mathbf{R}$, $\mathbf{a}$ and $\mathbf{n}$ is that the product of the eigenvalues of the matrix $\mathbf{G}^{-T}\mathbf{F}^T\mathbf{F}\mathbf{G}^{-1} \neq \mathbf{I}$ is equal to unity, which is satisfied for $\mathbf{F} = \mathbf{S}^0_1$ and $\mathbf{G} = \mathbf{S}^0_{-1}$. The resulting rotation $\mathbf{R}_1$ at the angle $\pi/2$ is illustrated in Fig. 4(b).

A more conventional case of misoriented coexisting patches of the original lattice (patches of the type 1-2) is shown in Fig. 4(c). Here the homogeneous deformation gradients correspond to the bottoms of the energy wells $\mathbf{S}^0$ and $\mathbf{S}^0_1$. They are microscopically compatible, however the associated micro-twin laminates were not observed and instead, we see in Fig. 4(c) macroscopically compatible but microscopically semi-coherent low-energy interface known as $\Sigma 5$ grain boundary [64], see Fig. 4(d). Despite the full stress relaxation inside the patches, here the apparently rigid rotation is again achieved through shear, see also [65] for related experimental observations.

To accentuate the inelastic mechanism of 'rotation by micro-twinning', shown Fig. 4(a,b), we used an artificial energy density which ensures that only one slip mechanism involving the energy wells $\mathbf{S}^0_1$ and $\mathbf{S}^0_{-1}$ is activated. Such bias can be achieved if we sufficiently strongly penalize volumetric distortions. The corresponding model is constructed in [54] and our Fig. 5(a) shows that it indeed produces an elongated effective yield surface favoring, under our loading protocol, only one slip mechanism. In Fig. 5(b) we show that during the avalanche in such a system an apparently rigid $\pi/4$ rotation develops behind a propagating transition front, which then separates the (rectangularly) stresses configuration $\mathbf{S}$ and the unstressed stable laminate involving the states $\mathbf{R}(\pi/2)\mathbf{S}^0_1$ and $\mathbf{S}^0_{-1}$, for transients see Movie S3 in [54]. Since the lattice scale micro-twinning is accomplished here through

the side motion of dislocations, the resulting rotation is an inelastic, dissipative process.

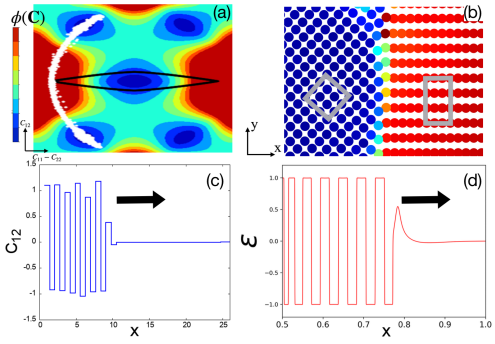


FIG. 5: The unfolding of the dislocation avalanche in the single-slip-biased version of the model. (a) Energy landscape showing the post-avalanche spreading of configurational points; (b) the structure of the moving front separating the initially stretched rectangular lattice and the growing micro-twinned (rotated) square lattice (colors indicate the level of energy); (c) the distribution of the shear strain $C_{12}$ across the transformation front shown in (b); (d) propagating front of lamination in the one dimensional toy model with parameters $\beta = 3 \times 10^{-6}$, $\eta = 0.0017$, $\gamma = 10^{-6}$, $A = -0.001$, see [54] for details.

An even more schematic, 1D description of a propagating transition front from Fig. 5(b), can be obtained if we neglect the transversal motion of dislocations and focus instead on the development of a laminate stabilized by competing interactions. To this end we can consider a toy potential $f(\epsilon) = (A/2)\epsilon^2 - (1/4)\epsilon^4 + (1/6)\epsilon^6$, where $\epsilon = u_x$. This potential can have up to three energy wells with the higher-symmetry state playing the role of the deformed configuration $\mathbf{S}$, and the two lower-symmetry states representing the symmetric variants $\mathbf{S}^0_1$ and $\mathbf{S}^0_{-1}$. Introducing viscoelastic dissipation, we obtain the dynamic equation $\eta u_{xxt} = -f''(u_x)u_{xx} + \beta u_{xxxx} + \gamma u$. Here $\eta$ is the viscosity coefficient, while the parameters $\beta$ and $\gamma$ represent lattice induced nonlocality and constraining elastic environment, respectively, see [54] for details. The numerical solution of this equation, modeling growth of a stable micro-laminate at the expense of an unstable homogeneous state [66], is compared in Fig. 5(c,d), see also Movie S4 in [54], with the corresponding inter-avalanche dynamics in the single-slip-biased version of our 2D model.

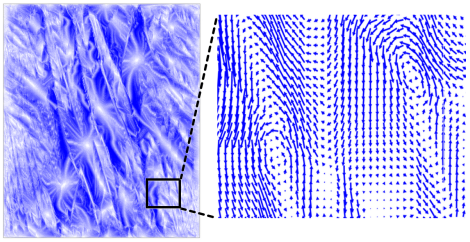

FIG. 6: Turbulent-like structure of the deformation field resulting from a dislocation avalanche. The displacement vectors connect pre- and post-avalanche positions of the individual nodes.

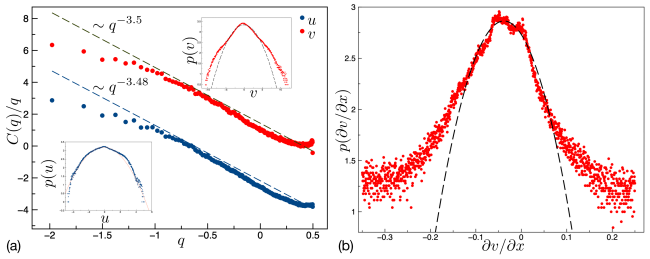


FIG. 7: (a) Fourier transform of auto-correlation function (power spectrum density) of the horizontal $u$ and vertical $v$ components of the displacement field; we interpret both components as surfaces which due to averaging are transitionally invariant and isotropic;the dashed lines show the power-law fit; insets show probability distributions $p(u)$ and $p(v)$. (b) Probability distribution $p(\partial v/\partial x)$ of the horizontal derivative of the displacement field exhibiting non-Gaussian wide tails.

In contrast to these intentionally simplified scenario, the original problem exhibits much larger complexity of the post-avalanche dislocation distribution. The availability in such a problem of a broad variety of low energy configurations, enabled by inelastic rotations, foments the development of imperfection-sensitive grain structure and makes plastic avalanches inherently unstable. To reveal the spatially intermittent nature of the deformation field in Fig. 6, we show in Fig. 6 the fluctuating part of the induced total nodal displacements $\mathbf{u}(\mathbf{x}) = \mathbf{y}(\mathbf{x}) - \mathbf{F}_{[]}(\alpha_c)\mathbf{x}$ with two correlated turbulent-type 'eddies' emphasized in the inset. In Fig. 7(a) we show the (radially averaged) power spectral density of the field $\mathbf{u}(\mathbf{x})$, illustrating the coexistence of a hierarchy of scales and revealing collective behavior of dislocations. The observed scaling $C(q)/q \sim q^{-2H-2}$, where $q = |\mathbf{q}|$, with noninteger (Hurst) exponent $H \approx 0.75$ indicates the self-affine (rough) nature of the surfaces representing the components of the displacement field which both exhibit the same fractal dimension $D = 3 - H \approx 2.25$ [67–70].

The robust algebraic tails in the probability distribution of displacement derivatives, shown in Fig. 7(b), are also strongly indicative of a quasi-turbulent nature of the distribution of plastic eddies in real space. For related observations in other models of crystal plasticity, see [71–74]; similarly complex turbulent-like motions involving vortex structures and scale free displacement fields have been recorded in granular flows [10, 75–77].

While the physical nature of the quasi-turbulence in crystal plasticity is clearly different from the classical inertial turbulence in fluids, the instability-driving nonlinearity may be as universal. Thus, the (quadratic) geometric nonlinearity is essential for capturing the finite rotations correctly [78–80]. The main constitutive nonlinearity of the energy density is also geometric as its main goal is to capture lattice invariant shears [81]. Similar to the case of high-Reynolds-number fluid turbulence, the model is conservative outside intermittent avalanches with dissipation remaining finite even as the microscopic viscosity tends to zero [82]. Furthermore, behind the

emerging scaling is the fact that in the limit $N \to \infty$ the governing equations of the model become scale-free. The parallel power law statistics of temporal correlations has been already obtained in the scalar version of the model [6].

To conclude, we used a novel mesoscopic approach to crystal plasticity to reveal the microscopic nature of the complex whirling motions involved in intermittent dislocation avalanches. Our analysis showed that behind the implied rotations are collective shears arising from dissipative motion of individual dislocations. The inherent instability of the underlying dynamics explains the quasi-turbulent nature of atomic displacements during the avalanches and suggests that the adequate description of plastic flows should be, as in fluids, probabilistic.

*Acknowledgments.* O. U. S. and R.B. were supported by the grants ANR-19-CE08-0010-01, ANR-20-CE91-0010, L. T. by the grant ANR-10-IDEX-0001-02 PSL.

[1] M. Zaiser, P. Moretti, and H. Chu, Adv. Eng. Mater. p. 1901208 (2019).
[2] M. Ovaska, A. Lehtinen, M. J. Alava, L. Laurson, and S. Zapperi, Phys. Rev. Lett. **119**, 265501 (2017).
[3] J. Weiss, W. B. Rhouma, T. Richeton, S. Dechanel, F. Louchet, and L. Truskinovsky, Phys. Rev. Lett. **114**, 105504 (2015).
[4] I. Groma, in *Mesoscale Models: From Micro-Physics to Macro-Interpretation*, edited by S. Mesarovic, S. Forest, and H. Zbib (Springer International Publishing, Cham, 2019), pp. 87–139.
[5] S. Papanikolaou, Y. Cui, and N. Ghoniem, Modell. Simul. Mater. Sci. Eng. **26**, 013001 (2017).
[6] P. Zhang, O. U. Salman, J. Weiss, and L. Truskinovsky, Phys Rev E **102**, 023006 (2020).
[7] A. H. Cottrell, in *Dislocations in Solids*, edited by F. R. N. Nabarro and M. S. Duesbery (Elsevier, 2002), vol. 11, pp. vii–xvii.
[8] W. Choi, Y. Chen, S. Papanikolaou, and J. Sethna, Computing in Science Engineering **14**, 33 (2012).
[9] J. P. Bouchaud, M. Mézard, and G. Parisi, Phys. Rev. E Stat. Phys. Plasmas Fluids Relat. Interdiscip. Topics **52**, 3656 (1995).
[10] F. Radjai and S. Roux, Phys. Rev. Lett. **89**, 064302 (2002).
[11] S. Odunuga, Y. Li, P. Krasnochtchekov, P. Bellon, and R. S. Averback, Phys. Rev. Lett. **95**, 045901 (2005).
[12] V. L. Berdichevsky, J. Mech. Phys. Solids **129**, 83 (2019).
[13] M. J. Marcinkowski, Phys. Status Solidi B Basic Res. **152**, 9 (1989).
[14] I. A. Kunin, Int. J. Theor. Phys. **29**, 1167 (1990).
[15] E. V. Shilko, Y. V. Grinyaev, M. V. Popov, V. L. Popov, and S. G. Psakhie, Phys Rev E **93**, 053005 (2016).
[16] J. S. Andrade, Jr, H. J. Herrmann, R. F. S. Andrade, and L. R. da Silva, Phys. Rev. Lett. **94**, 018702 (2005).
[17] R. Kulagin, Y. Beygelzimer, Y. Ivanisenko, A. Mazilkin, and H. Hahn, IOP Conf. Ser.: Mater. Sci. Eng. **194**, 012045 (2017).
[18] J. Oddershede, J. P. Wright, A. Beaudoin, and G. Winther, Acta Mater. **85**, 301 (2015).
[19] S. Hémery and P. Villechaise, Acta Mater. **171**, 261 (2019).
[20] J. P. Sethna, V. R. Coffman, and E. Demler, Phys. Rev. B Condens. Matter **67**, 184107 (2003).
[21] G. Winther, Materials Science and Engineering: A **483-484**, 40 (2008).
[22] F. P. E. Dunne, R. Kiwanuka, and A. J. Wilkinson, Proc. Math. Phys. Eng. Sci. **468**, 2509 (2012).
[23] G. M. Castelluccio and D. L. McDowell, Int. J. Plast. **98**, 1 (2017).
[24] A. Vinogradov and Y. Estrin, Prog. Mater Sci. **95**, 172 (2018).
[25] R. Arora and A. Acharya, Int. J. Solids Struct. **184**, 114 (2020).
[26] L. A. Zepeda-Ruiz, A. Stukowski, T. Oppelstrup, and V. V. Bulatov, Nature **550**, 492 (2017).
[27] A. V. Korchuganov, A. N. Tyumentsev, K. P. Zolnikov, I. Y. Litovchenko, D. S. Kryzhevich, E. Gutmanas, S. Li, Z. Wang, and S. G. Psakhie, J. Mater. Sci. Technol. **35**, 201 (2019).
[28] W.-S. Ko, A. Stukowski, R. Hadian, A. Nematollahi, J. B. Jeon, W. S. Choi, G. Dehm, J. Neugebauer, C. Kirchlechner, and B. Grabowski, Acta Mater. **197**, 54 (2020).
[29] N. Bertin, R. B. Sills, and W. Cai, Annu. Rev. Mater. Res. **50**, 437 (2020).
[30] J. Wang, A. H. M. Faisal, X. Li, Y. Hong, Q. Zhu, H. Bei, Z. Zhang, S. X. Mao, and C. R. Weinberger, J. Mater. Sci. Technol. **106**, 33 (2022).
[31] D. Barba, E. Alabort, S. Pedrazzini, D. M. Collins, A. J. Wilkinson, P. A. J. Bagot, M. P. Moody, C. Atkinson, A. Jérusalem, and R. C. Reed, Acta Mater. **135**, 314 (2017).
[32] J. Zhai, Z. Yan, and H. Yu, Nanoscale Adv. (2022).
[33] O. U. Salman and L. Truskinovsky, Phys. Rev. Lett. **106**, 175503 (2011).
[34] R. Baggio, E. Arbib, P. Biscari, S. Conti, L. Truskinovsky, G. Zanzotto, and O. U. Salman, Phys. Rev. Lett. **123**, 205501 (2019).
[35] J. L. Ericksen, Arch. Ration. Mech. Anal. **73**, 99 (1980).
[36] L. L. Boyer, Acta Crystallogr. A **45**, 29 (1989).
[37] I. Folkins, J. Math. Phys. **32**, 1965 (1991).
[38] J. Wang, S. Yip, S. R. Phillpot, and D. Wolf, Phys. Rev. Lett. **71**, 4182 (1993).
[39] B. W. Waal, Acta Crystallogr. A **46**, 17 (1990).
[40] E. Kaxiras and L. L. Boyer, Phys. Rev. B Condens. Matter **50**, 1535 (1994).
[41] S. Conti and G. Zanzotto, Arch. Ration. Mech. Anal. **173**, 69 (2004).
[42] O. U. Salman, R. Baggio, B. Bacroix, G. Zanzotto, N. Gorbushin, and L. Truskinovsky, C. R. Phys. **22**, 1 (2021).
[43] E. B. Tadmor, M. Ortiz, and R. Phillips, Philos. Mag. A **73**, 1529 (1996).
[44] J. Li, T. Zhu, S. Yip, K. J. Van Vliet, and S. Suresh, Materials Science and Engineering: A **365**, 25 (2004).
[45] R. L. Hayes, M. Fago, M. Ortiz, and E. A. Carter, Multiscale Model. Simul. **4**, 359 (2005).
[46] D. Rodney, Y. Le Bouar, and A. Finel, Acta Mater. **51**, 17 (2003).
[47] V. I. Levitas and M. Javanbakht, Phys. Rev. B Condens. Matter **86**, 140101 (2012).
[48] P. Biscari, M. F. Urbano, A. Zanzottera, and G. Zanzotto, J. Elast. **123**, 85 (2016).
[49] C. Denoual and A. Vattré, J. Mech. Phys. Solids **90**, 91

(2016).
[50] X. Hu, Y. Ji, L. Chen, R. A. Lebensohn, L.-Q. Chen, and X. Cui, Int. J. Plast. **143**, 103019 (2021).
[51] M. Ortiz and E. A. Repetto, J. Mech. Phys. Solids **47**, 397 (1999).
[52] S. Conti, G. Dolzmann, and C. Kreisbeck, in *Analysis and Computation of Microstructure in Finite Plasticity*, edited by S. Conti and K. Hackl (Springer International Publishing, Cham, 2015), pp. 31–62.
[53] J. L. Ericksen, Math. Mech. Solids **13**, 199 (2008).
[54] See Supplemental Material at [URL will be inserted by publisher] for details on the Projection on Pointcarré disk, the numerical implementation of the 1D model, and for captions to the Supplemental Movies 1–4. (2022).
[55] Y.-M. Juan and E. Kaxiras, Journal of Computer-Aided Materials Design **1**, 55 (1993).
[56] R. Sunyk and P. Steinmann, Int. J. Solids Struct. **40**, 6877 (2003).
[57] Y. Gao, Y. Wang, and Y. Zhang, IUCrJ **6**, 96 (2019).
[58] L. L. Boyer, Phys. Rev. B Condens. Matter **53**, 3145 (1996).
[59] M. Destrade, J. G. Murphy, and G. Saccomandi, Int. J. Non Linear Mech. **47**, 210 (2012).
[60] R. W. Ogden, *Non-linear elastic deformations. ellis horwood, chichester 1984* (1997).
[61] Y. Grabovsky and L. Truskinovsky, J. Nonlinear Sci. **23**, 891 (2013).
[62] D. L. Medlin, N. Yang, C. D. Spataru, L. M. Hale, and Y. Mishin, Nat. Commun. **10**, 1 (2019).
[63] M. Pitteri and G. Zanzotto, *Continuum models for phase transitions and twinning in crystals* (Chapman and Hall/CRC, 2002).
[64] Y. Gao, Materialia **9**, 100588 (2020).
[65] I. A. Ovid'ko and A. G. Sheinerman, Appl. Phys. Lett. **98**, 181909 (2011).
[66] W. van Saarloos, Phys. Rep. **386**, 29 (2003).
[67] K. R. Sreenivasan, Annu. Rev. Fluid Mech. **23**, 539 (1991).
[68] T. Y. Hou, X.-H. Wu, S. Chen, and Y. Zhou, Phys. Rev. E **58**, 5841 (1998).
[69] B. N. J. Persson, O. Albohr, U. Tartaglino, A. I. Volokitin, and E. Tosatti, J. Phys. Condens. Matter **17**, R1 (2005).
[70] C. Türk, A. Carbone, and B. M. Chiaia, Phys. Rev. E Stat. Nonlin. Soft Matter Phys. **81**, 026706 (2010).
[71] C. Fressengeas, A. J. Beaudoin, D. Entemeyer, T. Lebedkina, M. Lebyodkin, and V. Taupin, Phys. Rev. B Condens. Matter **79**, 014108 (2009).
[72] J. Chevy, C. Fressengeas, M. Lebyodkin, V. Taupin, P. Bastie, and P. Duval, Acta Mater. **58**, 1837 (2010).
[73] L. Angheluta, P. Jeraldo, and N. Goldenfeld, Phys. Rev. E Stat. Nonlin. Soft Matter Phys. **85**, 011153 (2012).
[74] Y. Beygelzimer, A. E. Filippov, R. Kulagin, and Y. Estrin (2021), 2111.05148.
[75] N. Oyama, H. Mizuno, and K. Saitoh, Phys. Rev. Lett. **122**, 188004 (2019).
[76] C. Goldenberg, A. Tanguy, and J.-L. Barrat, EPL **80**, 16003 (2007).
[77] T. Miller, P. Rognon, B. Metzger, and I. Einav, Phys. Rev. Lett. **111**, 058002 (2013).
[78] Y. Grabovsky and L. Truskinovsky, Continuum Mech. Thermodyn. **19**, 211 (2007).
[79] A. Finel, Y. Le Bouar, A. Gaubert, and U. Salman, C. R. Phys. **11**, 245 (2010).
[80] O. U. Salman, B. Muite, and A. Finel, Eur. Phys. J. B **92**, 20 (2019).
[81] O. U. Salman and L. Truskinovsky, Int. J. Eng. Sci. **59**, 219 (2012).
[82] G. Puglisi and L. Truskinovsky, J. Mech. Phys. Solids **53**, 655 (2005).

# Inelastic rotations and plastic turbulence (Supplementary Online Material)

R. Baggio,[1,2,3] O. U. Salman,[1] and L. Truskinovsky[2]

[1] *LSPM,CNRS UPR3407, Paris Nord Sorbonne Université, 93400, Villateneuse, France*
[2] *PMMH,CNRS UMR 7636 ESPCI ParisTech, 10 Rue Vauquelin,75005, Paris, France*
[3] *UMR SPE 6134, Université de Corse, CNRS, Campus Grimaldi, 20250 Corte, France*

(Dated: September 7, 2022)



*Energy density from interatomic potential.* Suppose that material points in a reference domain $\Omega_0$ undergo an affine deformation $y_i(\boldsymbol{x}) = x_i + u_i(\boldsymbol{x})$, where $u_i(\boldsymbol{x})$ is the displacement vector. The deformation gradient is then $F_{ij} = \partial y_i/\partial x_j = \delta_{ij} + \partial u_i/\partial x_j$, the metric tensor is $C_{ij} = F_{ki}F_{kj}$. To compute the energy density $\phi(\mathbf{C})$ we first define the relative position vectors between two atoms in the reference $R_i = x_i - x_i'$ and deformed $r_i = y_i - y_i'$ configurations. Then, since the deformation is affine, we have $r_i = F_{ij}R_j$ In case of pair interactions we can use the interatomic potential $V(\mathbf{r}) = V(r)$, where r is the distance between the atoms and, in particular, in the $2D$ case, it reduces to $V(\sqrt{R_1^2C_{11} + 2R_1R_2C_{12} + R_2^2C_{22}})$. The strain energy density $\phi(\mathbf{C})$ averaged over the domain $\Omega_0$ can be written as a sum

$$\phi(\mathbf{C}) = \frac{1}{\Omega_0}\sum_{\boldsymbol{x}}\sum_{\boldsymbol{x'}\in\mathcal{N}(\boldsymbol{x})} V\Big(\sqrt{R_iC_{ij}R_j}\Big), \tag{1}$$

where the internal summations involves all $\boldsymbol{x'}$ belonging to the cutoff neighborhood $\mathcal{N}(\boldsymbol{x})$. In our numerical experiments we used the potential

$$V(r) = -2/e^{-8(-1.425+r)^2} - 2/e^{-8(-1+r)^2} + 2/r^{12} \tag{2}$$

constructed in [1]. In order to perform the sum in (1), we used the reference square lattice composed of $8\times 8$ atoms with the lattice distance $r_0 = 1.0658$. In view of the global symmetry, it is sufficient to construct the potential $\phi(\mathbf{C})$ in the minimal periodicity domain $D = \{0 < C_{11} \le C_{22}, \quad 0 \le C_{12} \le C_{11}/2\}$. Then we can use the appropriate symmetry transformations $\mathbf{m}$ to map an arbitrary metric tensor $\mathbf{C}$ on its prototype in $D$. This is achieved by replacing $\mathbf{C}$ in (1) with its reduced version $\tilde{\mathbf{C}} = \mathbf{m}^T\mathbf{C}\mathbf{m}$.

*Projection on Poincaré disk.* Configurational space $\det\mathbf{C} = 1$ is a hyperboloid described by the equation $C_{11}C_{22} - C_{12}^2 = 1$. In Fig. 1(a) of the main text the tessellation of this configurational space into invariant subdomains is illustrated using the projection onto the Poincaré disk which is bounded by a circle of unit radius. In this mapping the point $(x, y)$ on the disk represents the point $(\widehat{x}, \widehat{y}, \widehat{z}) = ((C_{11} - C_{22})/2, C_{12}, (C_{11} + C_{22})/2)$ on the hyperbolic surface with

$$x = \frac{(\frac{C_{12}}{C_{22}})^2 + (\frac{1}{C_{22}})^2 - 1}{(\frac{C_{12}}{C_{22}})^2 + ((\frac{1}{C_{22}}) + 1)^2}, \tag{3}$$

$$y = \frac{2(\frac{C_{12}}{C_{22}})}{(\frac{C_{12}}{C_{22}})^2 + ((\frac{1}{C_{22}}) + 1)^2}. \tag{4}$$

We recall that in these relations, once $C_{22}$ and $C_{12}$ are given, the component $C_{11}$ is determined by the condition $C_{11}C_{22} - C_{12}^2 = 1$.

*Evolving lattice configuration.* In Fig. 1 (a,b,c) we show the snapshots of the evolving lattice configuration in the fast numerical time of the system-size avalanche. The spreading of the corresponding cloud of configurational points in the space of metric tensors is illustrated in Fig. 1 (d,e,f).

The system was loaded quasi-statically in a hard device by applying on the boundary affine deformation $\mathbf{F}_{\square}(\alpha)$. In homogeneous response, such mapping transforms squares into rectangles. After the instability, many of the rectangularily stretched elements snaps back to the reference energy well $\mathbf{S}$ but a significant percentage of elements also ends up in the two symmetric energy wells $\mathbf{S}_1^0 = \mathbf{F}(1, 0)$ and $\mathbf{S}_{-1}^0 = \mathbf{F}(-1, 0)$ which corresponds to the activation of single slip plasticity. The other two symmetric energy wells $\mathbf{S}_1^{\pi/2} = \mathbf{F}(1, \pi/2)$ and $\mathbf{S}_{-1}^{\pi/2} = \mathbf{F}(-1, \pi/2)$ also get populated but only at the end of the avalanche, indicating that the second main slip system is now also activated.

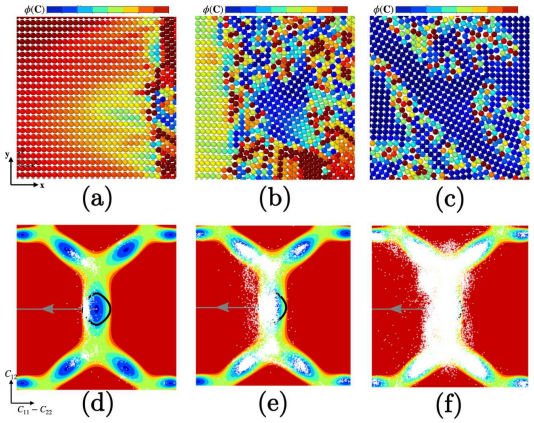


FIG. 1. The unfolding of a dislocation avalanche: (a,b,c) in real space (colors indicate the level of strain energy density), (d,e,f) in the configurational space of metric tensors. Large red/yellow region in (a) corresponds to elastically stressed homogeneous rectangular configuration of the original lattice. Large blue cells in (c) correspond to symmetry related versions of unstressed square lattices. White dots in (d,e,f) show the progressive spreading of the configurational points representing individual elastic elements. The dark ovals show the effective yield surfaces around the energy well corresponding to pristine crystal

*Molecular statics simulations.* To test the basic predictions of the mesoscale model we also performed the parallel molecular statics simulations. The role of elastic elements in such simulations was played by individual atoms. In the corresponding numerical experiments the positions of the atoms for the given boundary conditions were determined by minimizing the total potential energy of a system composed of $N_A$ atoms. It can be written in the form $\Pi = W^{int} - W^{ext}$, where the internal energy is $W^{int} = \frac{1}{2}\sum_{\alpha}^{N_A}\sum_{\beta,\beta\neq\alpha}^{N_A} V(r^{\alpha\beta})$, while the external energy of the loading device is $W^{ext}$, which will vanish in our case since we use hard device boundary conditions to mimic the loading protocol of the mesoscopic model. The interatomic potential is taken to be the same as in the mesoscopic theory $V(r^{\alpha\beta})$ where $r^{\alpha\beta}$ is the distance between the atoms $\alpha$ and $\beta$. The equilibrium positions of the atoms were found by solving the equations $d\Pi/d\mathbf{r}^{\lambda} = 0$, where $\lambda = 1, \ldots, N_A$. To solve the equilibrium equations we used the L-BFGS algorithm [2] which builds a positive definite linear approximation of these equations allowing one to make a quasi-Newton step lowering the total energy $\Pi$. In order to impose the hard device type boundary conditions in molecular statics experiments, which were also used in the mesoscale model, we applied affine displacements (of a pure shear type) to the atoms within the boundary layer of a small thickness. The amplitude of the loading was incrementally increased and kept fixed during each relaxation step. Similar to the experience with the mesoscopic modeling, in the parallel molecular statics test the pristine crystal was deforming homogeneously till the critical value of the loading parameter $\alpha$ was reached at which the system size plastic avalanche took place. In Fig. 2 we present a fragment of a post avalanche configuration showing the typical grain structure with disoriented micro-twinned domains which are practically unloaded while the energy is localized on the highly dislocated inter-grain boundaries. The inset shows a magnified version of the apparent $\pi/2$ rotation of a grain with respect to the original square lattice. Other differently oriented patches are visible as well forming a complex crystallographic texture. The overall picture is very similar to the one obtained in the mesoscopic model which corroborates its basic predictions. In this Letter we do not perform quantitative comparison that would require the discussion of the role of the internal scales in the two models.

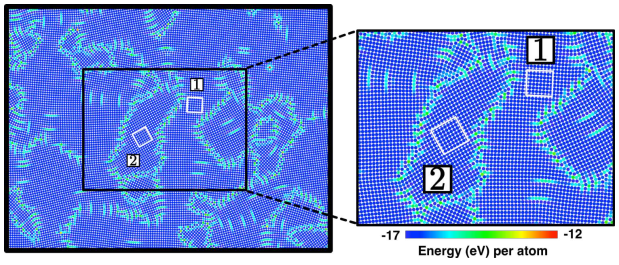


FIG. 2. Final positions of the atoms in a molecular statics experiment following the system size plastic avalanche. Atoms are colored according to the level of their potential energy: red-high, blue-low. The magnification shows the inelastically rotated (micro-twinned) domains representing the unloaded square lattice coexisting with slightly (elastically) rotated original square lattice. These low energy domains are separated by high-energy dislocation-rich interfaces.

*Solution of the twinning equation.* Suppose that the constant deformation gradients $\mathbf{G}$ and $\mathbf{F}$ correspond to two equivalent minima of the strain-energy $\phi(\mathbf{C})$. To generate piece wise affine continuous deformation, across an invariant discontinuity plane they must satisfy on such a plane the kinematic (Hadamard) compatibility conditions [3]:

$$\mathbf{RF} = \mathbf{G} + \mathbf{a} \otimes \mathbf{n}^* = \mathbf{G}\left(\mathbf{I} + \mathbf{a}^* \otimes \mathbf{n}^*\right) = \left(\mathbf{I} + \mathbf{a} \otimes \mathbf{n}\right)\mathbf{G} \tag{5}$$

where $\mathbf{R} \in SO(2)$ is a rotation. The Eulerian vector $\mathbf{a}$ (normal to the discontinuity plane) and covector $\mathbf{n}$ must satisfy $\mathbf{a} \cdot \mathbf{n} = 0$; their Lagrangian counterparts are $\mathbf{a}^* = \mathbf{G}^{-1}\mathbf{a}$ and $\mathbf{n}^* = \mathbf{G}^T\mathbf{n}$. If we assume further that $\det \mathbf{F} = \det \mathbf{G} = 1$ and exclude reflections, the deformation gradients satisfying (5) form a mechanical twin. If, in addition, the rotation $\mathbf{R}$ belongs to the point group of the lattice, such twinning structure produces the undistorted zero energy configuration. This is what happens in the case when $\mathbf{F} = \mathbf{S}_1^0$, $\mathbf{G} = \mathbf{S}_{-1}^0$. The resulting microtwinned laminates are sometimes referred to as *pseudotwins* [3].

The twinning equation (5) was studied extensively, see for instance [4]. It was shown that (5) admits either no solutions or two solutions. The two solutions exist when the matrix $\mathbf{G}^{-T}\mathbf{F}^T\mathbf{F}\mathbf{G}^{-1} \neq \mathbf{I}$ and its ordered eigenvalues $\mu_1 < \mu_2$ are such that $\mu_1\mu_2 = 1$. In that case, the two solutions are given explicitly by the formulas:

$$\mathbf{a} = \rho\left(\sqrt{\frac{\mu_2(1-\mu_1)}{\mu_2-\mu_1}}\mathbf{v}_1 + \kappa\sqrt{\frac{\mu_1(\mu_2-1)}{\mu_2-\mu_1}}\mathbf{v}_2\right), \tag{6}$$

$$\mathbf{n} = \frac{1}{\rho}\left(\frac{\sqrt{\mu_2}-\sqrt{\mu_1}}{\sqrt{\mu_2-\mu_1}}\right)\left(-\sqrt{1-\mu_1}\mathbf{v}_1 + \kappa\sqrt{\mu_2-1}\mathbf{v}_2\right), \tag{7}$$

where $\hat{\mathbf{v}}_1$ and $\hat{\mathbf{v}}_2$ are the normalized eigenvectors of $\mathbf{G}^{-T}\mathbf{F}^T\mathbf{F}\mathbf{G}^{-1}$, $\rho > 0$ is a constant ensuring that $|\mathbf{n}| = 1$ and $\kappa = \pm 1$. Once $\mathbf{a}$ and $\mathbf{n}$ are known, the rotation $\mathbf{R}$ can be obtained directly from (5).

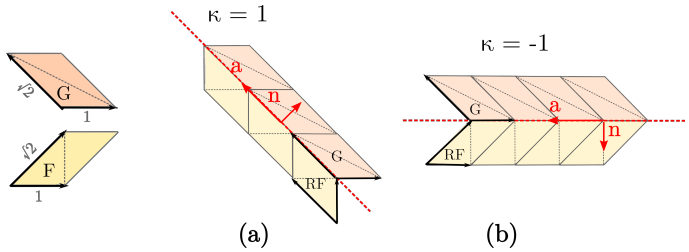


FIG. 3. The two solutions of the twinning equation (5) for the deformation gradients $\mathbf{F} = \mathbf{S}_1^0$ and $\mathbf{G} = \mathbf{S}_{-1}^0$.

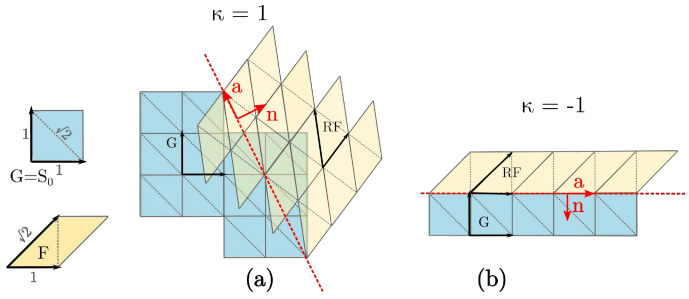


FIG. 4. The two solutions of the twinning equation (5) for the deformation gradients $\mathbf{F} = \mathbf{S}_1^0$ and $\mathbf{G} = \mathbf{S}^0 = \mathbf{I}$.

For the case when $\mathbf{F} = \mathbf{S}_1^0$ and $\mathbf{G} = \mathbf{S}_{-1}^0$ the solution corresponding to $\kappa = 1$ is the one observed in the post-instability patchy pattern. It is characterized by the parameters

$$\mathbf{a}^T = \{-\sqrt{2}, \sqrt{2}\} \quad \mathbf{n}^T = \{\cos\zeta, \sin\zeta\} \quad \zeta = \pi/4 \tag{8}$$

with $\mathbf{R}$ a counter-clockwise rotation of $\psi = 2\zeta = \pi/2$. For $\kappa = -1$, the solution is different

$$\mathbf{a}^T = \{-2, 0\} \quad \mathbf{n}^T = \{\cos\zeta, \sin\zeta\} \quad \zeta = -\pi/2 \tag{9}$$

with $\mathbf{R}(\psi = 0)$, see Fig. 3. The corresponding micro-twins were not observed in our simulations.

Another type of microstructure, observed in our simulation results, corresponds to the case when $\mathbf{G} = \mathbf{S}^0$ and $\mathbf{F} = \mathbf{S}^0_1$. The two solutions with $\kappa = -1$ and $\kappa = 1$ are, see Fig. 4:

$$\kappa = 1; \quad \mathbf{a}^T = \{-\sin\zeta, \cos\zeta\}, \tag{10}$$

$$\mathbf{n}^T = \{\cos\zeta, \sin\zeta\}, \quad \mathbf{R}(2\zeta), \quad \zeta = \arctan(1/2) \tag{11}$$

$$\kappa = -1; \quad \mathbf{a}^T = \{1, 0\}, \tag{12}$$

$$\mathbf{n}^T = \{\cos\zeta, \sin\zeta, \} \quad \mathbf{R}(\psi = 0), \quad \zeta = -\pi/2, \tag{13}$$

The solution associated corresponding to $\kappa = 1$ was observed in our post-avalanche patchy pattern, while the solution corresponding to $\kappa = -1$ was not.

*Polynomial energy density.* The energy density, which we used in the main text to obtain Figs. 5(a-b), is chosen to ensure an independent control of volumetric and deviotoric contributions. To this end, it is taken in the additive form

$$\phi(\mathbf{C}) = \phi_v(\det\mathbf{C}) + \phi_d(\mathbf{C}/(\det\mathbf{C})^{1/2}). \tag{14}$$

We took the volumetric part in the artificial form $\phi_v(s) = \mu(s - \log(s))$ (with $\mu = 25$) which precludes physically anticipated softening in tension but still bans configurations with infinite compression. As we explained in the main text, the volume preserving term $\phi_d$ needs to be specified only inside a single domain of periodicity and then extended by global symmetry. Inside such a domain we used for $\phi_d$ the lowest order polynomial expression which which ensures the global continuity of the elastic moduli. More specifically, we used the expression first proposed in [5]:

$$\phi_d(\tilde{\mathbf{C}}) = \beta\psi_1(\tilde{\mathbf{C}}) + \psi_2(\tilde{\mathbf{C}}) \tag{15}$$

where $\psi_1 = {I_1}^4\, I_2 - 41\, {I_2}^3/99 + 7\, I_1\, I_2\, I_3/66 + {I_3}^2/1056$, and $\psi_2 = 4\, {I_2}^3/11 + {I_1}^3\, I_3 - 8\, I_1\, I_2\, I_3/11 + 17\, {I_3}^2/528$. The (hexagonal) invariants here have the structure: $I_1 = \frac{1}{3}(\tilde{C}_{11} + \tilde{C}_{22} - \tilde{C}_{12})$, $I_2 = \frac{1}{4}(\tilde{C}_{11} - \tilde{C}_{22})^2 + \frac{1}{12}(\tilde{C}_{11} + \tilde{C}_{22} - 4\tilde{C}_{12})^2$, and $I_3 = (\tilde{C}_{11} - \tilde{C}_{22})^2(\tilde{C}_{11} + \tilde{C}_{22} - 4\tilde{C}_{12}) - \frac{1}{9}(\tilde{C}_{11} + \tilde{C}_{22} - 4\tilde{C}_{12})^3$. The choice $\beta = -1/4$ enforces the square symmetry on the reference state. Importantly, it is not the particular structure of $\phi_d$ which is fully controlled by symmetry, but rather the assumption regarding $\phi_v$ that is ultimately responsible for getting the highly elongated effective 'yield surface'.

*1D prototypical model.* Consider a continuum 1D system described by a scalar displacement field $u(x)$ where $0 \leqslant x \leqslant L$. The energy of the system is taken in the form

$$E = \int_0^1 [f(u_x) + \frac{\beta}{2}u_{xx}^2 + \frac{\gamma}{2}u^2]dx, \tag{16}$$

where the first term $f(u_x)$ represents a triple well potential depending on the strain variable $\epsilon = u_x$. The higher order second term $u_{xx}$ depends on the strain gradient $\epsilon_x = u_{xx}$ and brings the internal length scale. The last term $u^2$, representing the energy of the constraining elastic environment, brings another (competing) length scale into the problem. Introducing the Rayleigh type dissipation

$$R = \frac{\eta}{2}\int_0^1 \dot{u}_x^2 dx, \tag{17}$$

we obtain the main dynamic equation used in the main text

$$\eta u_{xxt} = -f''(u_x)u_{xx} + \beta u_{xxxx} + \gamma u. \tag{18}$$

To solve this equation numerically, we first approximate spatial derivatives by finite differences using a fixed grid with size $h$ and utilize semi-implicit forward Euler discretization in time with a time step $\mathrm{d}t$. The resulting discrete set of equations in Fourier space takes the form

$$\hat{u}^{t+\mathrm{d}t}(q) = \frac{\eta\hat{M}_3(q)\hat{u}^t(q) - \mathrm{d}t\hat{M}_1(q)\hat{f}'(q)}{\eta\hat{M}_3(q) - \mathrm{d}t(\beta\hat{M}_2(q) + \alpha)}, \tag{19}$$

where $\hat{M}_1(q) = i\sin(q)/(2h)$, $\hat{M}_2(q) = 16\sin(q)^4/h^4$ and, $\hat{M}_3(q) = (2\cos(q) - 2)/h^2$. The nonlinear function $f' = \partial f/\partial u_x$ is first evaluated in real space and then Fourier transformed to obtain $\hat{f}'(q)$. The discrete Fourier transform

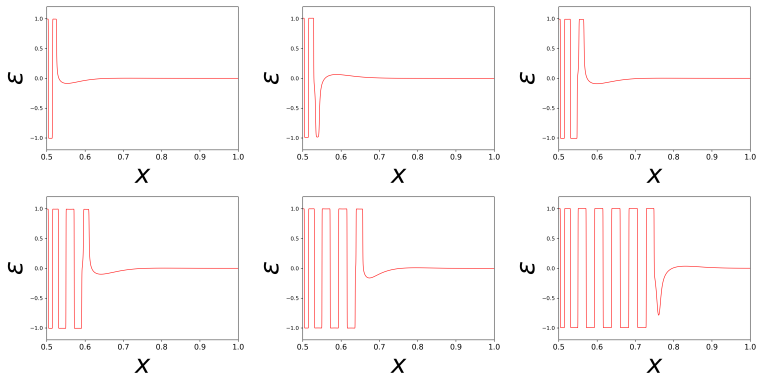


FIG. 5. Evolution of the strain field $\epsilon(x)$ at times $t = 390, 480, 580, 760, 970, 1350 \times \mathrm{d}t$. The system ultimately evolves to the fully transformed state, which is a mixture of $\epsilon(x) \approx \pm 1$.

on a unit grid is defined as $\hat{u}(q) = N^{-1} \sum_{\mathrm{i}} u_{\mathrm{i}} e^{-iqx}$ with $x = \mathrm{i}$ and $q = 2\pi \mathrm{k}/N$, where $\mathrm{i} = 0, 1, ..., N-1$ and, $\mathrm{k} = 0, 1, ..., N-1$. In our simulations, we used the parameter values: $h = 0.04$, $N = 8192$, the time step $\mathrm{d}t = 0.004$, $\beta = 3 \times 10^{-6}$, $\eta = 0.0017$ and $\alpha = 10^{-6}$. The initial data were chosen in the form a localized strain increment $\epsilon(x) = 0.5 e^{-(x-x_m)^2}$ centered around $x_m = 0.5$. The Fourier image of the corresponding displacement field is $\hat{u}(q) = \hat{\epsilon}(q)/\hat{M}_1(q)$ for $q \neq 0$. The time evolution of the resulting strain field $\epsilon(x,t)$ is shown in Fig. 5.

*Supplemental movies.* The first three movies reveal the fast time dynamics behind the plastic avalanche starting from the loss of stability of a homogeneous state at a critical load and until the equilibrium post-avalanche pattern is reached.

**Movie S1** : the deformation field $\mathbf{y}(\mathbf{x})$;

**Movie S2** : the non-affine displacement field : $\mathbf{u}(\mathbf{x}) = \mathbf{y}(\mathbf{x}) - \mathbf{F}_{\square}(\alpha_c)\mathbf{x}$;

**Movie S3** : the evolution of the deformation field $\mathbf{y}(\mathbf{x})$ in the case of an artificial polynomial strain-energy density. The forth movie shows the time evolution of the strain field in the prototypical 1D model

**Movie S4** : The field $\epsilon(x,t)$ showing the growth of a lamainate starting from an initial strain inhomogeneity.

[1] L. L. Boyer, Phys. Rev. B Condens. Matter **53**, 3145 (1996).
[2] S. Bochkanov and V. Bystritsky, Available from: www alglib net (2013).
[3] M. Pitteri and G. Zanzotto, *Continuum models for phase transitions and twinning in crystals* (Chapman and Hall/CRC, 2002).
[4] A. Forclaz, J. Elast. **57**, 281 (1999).
[5] S. Conti and G. Zanzotto, Arch. Ration. Mech. Anal. **173**, 69 (2004).